Automatic Layer Line Marking on HRTEM Images of Catalysts Based on Tracing Consistent Responses of Gabor Filters

Andrey Kopylov[1,2][0000-0003-3193-583X], Oleg Seredin[1,2][0000-0003-0410-7705] and Evgenii Semenishchev [2][0000-0001-9817-0021]

[1] Tula State University, Tula, Russian Federation
[2] Moscow State University of Technology «STANKIN», Moscow, Russian Federation
and.kopylov@gmail.com

Abstract. This paper presents a method for the automated marking of linear features in high-resolution transmission electron microscopy (HRTEM) images of sulfide catalysts, based on tracing consistent responses from a Gabor filter bank. The method addresses the critical need for quantitative assessment of morphological parameters of the active phase nanoparticles specifically, average slab length and stacking number which directly affects the catalytic performance of Co- or Ni-promoted MoS_2/WS_2 systems. The algorithm comprises: application of a multi-orientation Gabor filter bank to detect linear structures; Otsu-based adaptive threshold segmentation; filtering and recursive partitioning of complex, non-convex regions via bottleneck detection; dynamic programming-based tracing of individual layers with frequency-driven initialization; and merging of overlapping regions from adjacent filter orientations using a minimum spanning tree construction. The approach does not require training on large annotated datasets and relies on physically grounded assumptions regarding the periodicity of layered structures. Experimental evaluation against expert-annotated images yielded an F1-score of 0.83. The proposed framework can serve as a baseline for comparative studies and is readily adaptable to the analysis of other quasi-periodic linear microstructures.

Keywords: Computer Vision, Electron Microscopy, Sulfide Catalysts, Automated Image Annotation, Gabor filters, Line Tracing, Nanoparticle Morphology Analysis.

1 Introduction

With the widespread use of high-resolution transmission electron microscopy (HRTEM) for characterizing the morphology of nanostructured materials in chemistry and biology, the task of automated analysis and interpretation of HRTEM images becomes critically important [1].

In the analysis of catalysts whose active phase consists of molybdenum or wolfram disulfide nanocrystallites promoted with cobalt or nickel [2, 3], the resulting images exhibit a characteristic appearance (Fig. 1) dictated by a layered structure in which single molybdenum or tungsten layers are sandwiched between two closely packed sulfur anion layers. The threadlike fringes observed in HRTEM micrographs effectively represent MoS_2/WS_2 layers whose basal planes are oriented parallel to the electron beam [4]. An isolated fringe or a group of parallel fringes corresponds to catalyst nanoplatelets with spatial periodicity and varying orientations. According to current understanding, the catalytic activity of such systems depends on the morphology of the active phase particles, specifically the average slab length and the number of slab layers (stacking number) [5].

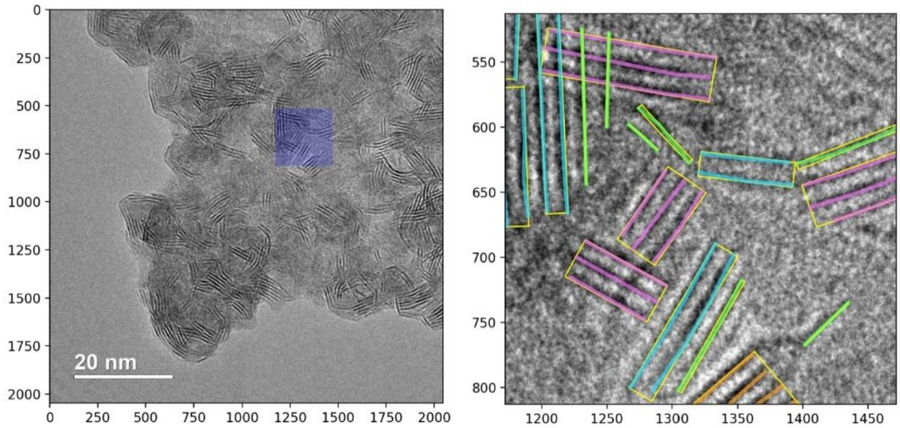

Fig. 1. HRTEM image of $NiMoS_{0.5}$ catalysts (left) and expert labeling of stacked layers (right)

Traditionally, these parameters are determined manually by experts, a process that demands considerable time, effort, and sustained concentration. To date, we have found no examples in the scientific literature of automated analysis for such images. Furthermore, publicly available, standardized datasets containing TEM images of sulfide catalysts with annotated sulfide stacking layers are absent. Most catalytic studies [6, 7] rely on proprietary data.

The most relevant approaches appear to originate from the field of image-based nanocrystallography (IBN), particularly the Lattice Fringe Fingerprinting method [8, 9]. These techniques are based on analyzing fringes corresponding to crystal lattice planes, which arise from phase contrast effects. Visually, such patterns indeed resemble micrographs of layered sulfide particles (Fig. 2a). However, directly adapting these algorithms for sulfide catalysts proves unfeasible. In polymers, for which these methods were originally developed, segmentation relies on the thinness of the fringes and their spatial continuity (Fig. 2b). The nanoplatelets of the catalyst active phase exhibit a distinct morphology: in micrographs, they manifest as layered structures with parallel, often curved fringes containing packing defects and varying stacking arrangements (Fig. 2c). Their analysis requires alternative methodologies, such as direct statistical processing of HRTEM images [6, 7, 10, 11].

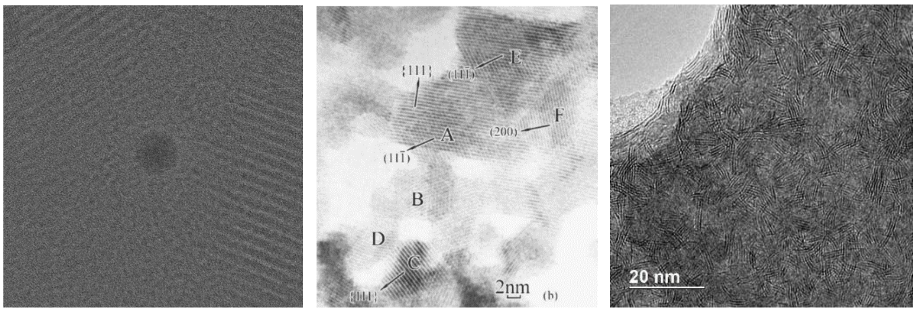

(a) (b) (c)

Fig. 2. (a) HRTEM image of the six WC_{1-x} nanocrystals from [8], (b) HRTEM image of a conjugated polymer from [9], (c) TEM image of *in situ* prepared $NiMoS_{0.5}$ catalysts [7].

Given the high number of target objects per micrograph and the ambiguity inherent in human perception of such structures, manual detection is exceedingly labor-intensive. Automating this task initially requires solving the problem of detecting individual lines corresponding to layers across the image and subsequently grouping these lines into structures representing sulfide nanoparticles. Two primary strategies emerge for addressing these tasks. The first approach involves detecting image regions corresponding to individual particles, followed by identifying the lines (layers) within those regions. Consequently, the second task is reduced to region detection. The second strategy reverses this order: individual lines (layers) are first detected across the entire image and then clustered into multi-layered particles. Lines that cannot be grouped with others correspond to single-layer particles.

The first strategy aligns better with human perception—experts typically localize entire nanoparticles first and then count the layers within them. This strategy forms the focus of the present work.

To detect particles with varying spatial orientations, a Gabor filter bank corresponding to 12 directions is employed.

Inevitable noise and distortions in electron microscopy images can generate complex, non-convex regions that require partitioning into near-convex components and filtering out regions with excessively small areas. Within each identified region, layer detection and tracing are performed using frequency analysis and dynamic programming.

Since layers within a single particle may be curved, significant filter responses across multiple directions can occur within the same particle region. We developed a method to merge such overlapping regions based on constructing a minimum spanning tree (MST) on vertices of partially overlapping lines.

The proposed method constitutes a novel and original contribution to nanomaterial analysis. It requires no large training datasets and is grounded in physically justified assumptions regarding the periodicity and orientation of layered structures. The developed framework can serve as a baseline for future comparative studies.

Images with similar structural characteristics exist outside the scope of electron microscopy. Examples are provided in Fig. 3.

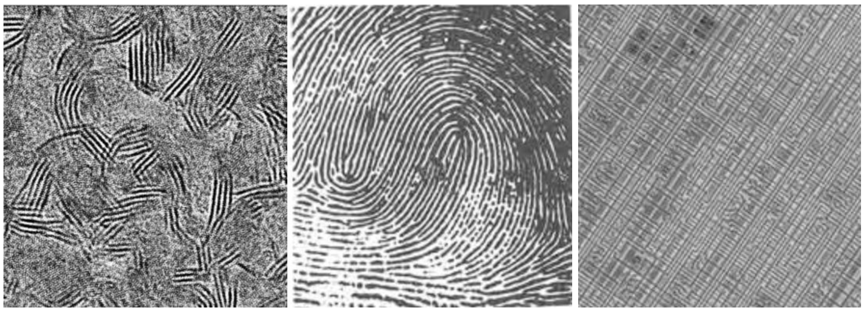

(a) (b) (c)

Fig. 3. Similar structured images (a) HRTEM image of catalysts, (b) Fingerprint image, (c) Circuit board.

The proposed methods can also be adapted for such images, thereby extending the applicability of the approach.

2 Construction and Application of a Gabor Filter Bank

Manual annotation of such micrographs is an extremely labor-intensive process requiring substantial time and high expert qualification. This significantly complicates the use of powerful analytical tools such as deep learning models, particularly convolutional neural network architectures that have proven effective in image segmentation. This motivated us to employ classical computer vision methods that rely on model-based representations of image structure rather than data-driven learning. Two-dimensional Gabor filters [12] are widely used for detecting linear features oriented at various angles.

The interlayer distance is constant and determined by the material's physical properties. For instance, in the Inorganic Crystal Structure Database (ICSD) [8], the lattice parameter $c$of molybdenum disulfide is ≈ 12.3–12.9 Å, yielding an interlayer spacing of approximately 0.615–0.645 nm. This allows a priori determination of the primary frequency for the Gabor filters, denoted as f_{gabor}.

We employ a Gabor filter bank comprising filters at $\theta_k = k\pi / N_\theta, k = 0, ..., N_\theta - 1$ orientations. The filter response is calculated through convolution. The processing results for the first two θ values are shown in Fig. 4.

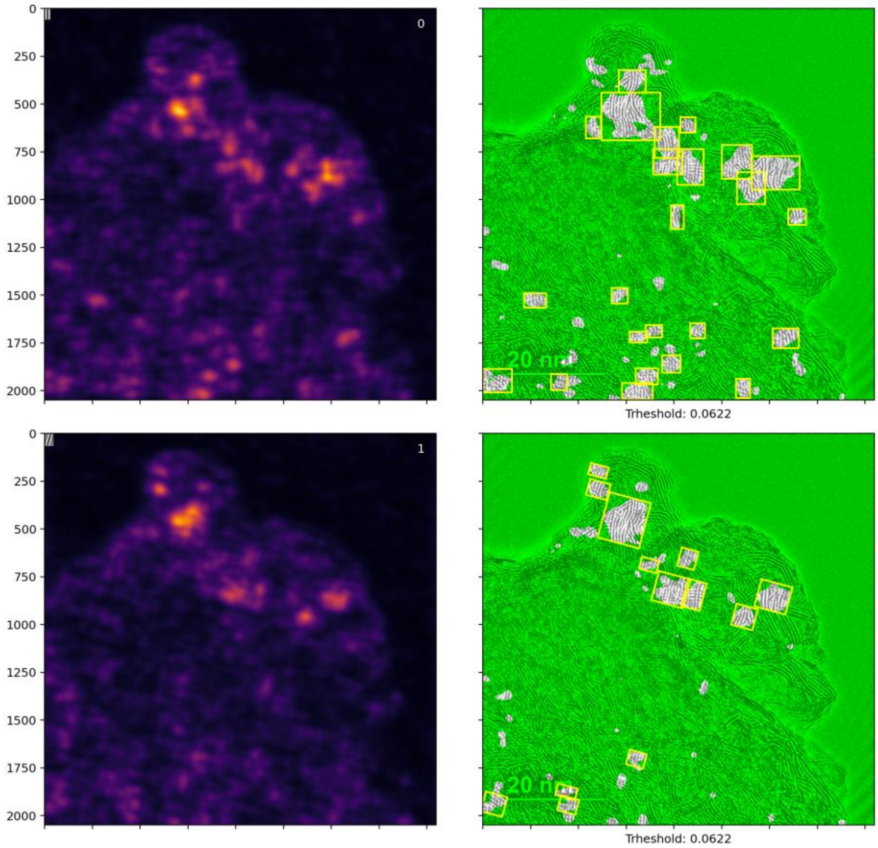

Fig. 4. Filter responses for the first two orientations (left) and detected candidate particle regions (right).

This stage produces a response tensor $\mathbf{G} \in \mathbb{R}^{N_\theta \times H \times W}$.

3 Threshold Segmentation, Filtering, and Partitioning of Complex Regions

Binary masks $M_j^{(k)}$ are generated from tensor $\mathbf{G}$, where $k = 0,...,N_\theta - 1$ is the filter index and j denotes the region index. An adaptive threshold τ is determined using Otsu's method and scaled by a coefficient k_{thresh}. The resulting connected components (regions) are filtered by a minimum area $A_{\min}$.

Regions with complex geometries (e.g., two particles connected by a narrow bridge) are partitioned using a bottleneck detection algorithm [13–15].

Let $\mathcal{C} = \{\mathbf{p}_0, \mathbf{p}_1, \ldots, \mathbf{p}_{n-1}\}$ be an ordered set of n $n$points constituting the external contour of a connected region on a binary image B, where $\mathbf{p}_i = (x_i, y_i)$.

The algorithm iterates over point pairs $(\mathbf{p}_i \mid \mathbf{p}_j)$ on this contour and computes a bottleneck metric R_{ij}, defined as the ratio of the shortest path length along the contour to the direct Euclidean distance between them. A high R_{ij} value indicates that the points are spatially close but distant along the contour, a characteristic signature of a "neck" between two object components.

Consequently, we obtain the coordinates of two points whose connection represents the optimal cutting position to split a complex object. A 4-connected line is drawn through these points, and the component is relabeled. This procedure is applied recursively to the resulting sub-regions until no further candidates for partitioning remain.

4 Tracing of Individual Layers

Individual layer reconstruction is performed within each region. An example of the procedure is shown in Fig. 5.

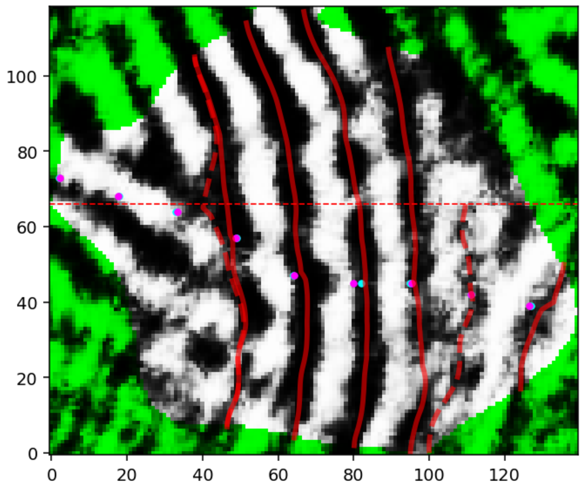

Fig. 5. – Example of layer tracing in a nanoscale particle. Dots indicate starting positions for the tracing procedure; the horizontal dashed line corresponds to the image row with maximum variance; vertical dashed lines indicate false layers discarded during analysis.

The source image and the region's binary mask are extracted via the bounding box and rotated by an angle corresponding to the direction θ_k the Gabor filter that generated the region. The resulting normalized images are denoted I_{rot} and M_{rot} with dimensions $H \times W$, where the coordinate axes are aligned with the dominant structural orientation.

To locate the transverse coordinate y^* with maximum textural activity, the row-wise intensity variance is computed within the region mask. To enhance robustness, subsequent analysis is conducted in the neighborhood $\mathcal{N}_y = [y^* - \delta, y^* + \delta]$, where δ is a small value (e.g., 3).

The averaged transverse intensity profile $\overline{I}(x)$ is computed by column-wise averaging within $\mathcal{N}_y$. A discrete Fourier transform with low-frequency component suppression is applied to the profile to mitigate global illumination gradients.

The dominant spatial frequency u^* is identified by detecting local maxima in the amplitude spectrum, followed by selecting the harmonic closest to the a priori Gabor filter frequency estimate f_{gabor} :

$$u^* = \underset{u \in \mathcal{L}_{max}}{\arg\min} \left| u - f_{gabor} W \right| .$$

u^* determines the line width $w_l = W / u^*$, while the corresponding phase component φ^* defines the initial grid offset.

The initial horizontal coordinates are generated as a uniform grid with step w_l and phase correction:

$$x_k^{(0)} = \frac{w_l}{2}\left(1 - \frac{\varphi^*}{\pi}\right) + k \cdot w_l, k \in \mathbb{Z}, x_k^{(0)} < W .$$

Vertical coordinates are initialized with the y^* value, then performed by locating the maximum response of the rotated Gabor filter G_{rot} :

$$y_k^{(0)} = \arg\max_y G_{rot}\left(y, x_k^{(0)}\right) .$$

Final line center localization is achieved by searching for a minimum local intensity within a horizontal window of width w_l on row $y_k^{(0)}$. The coordinate x_k^* is selected as the minimum position nearest to $x_k^{(0)}$, ensuring robustness against noise in the presence of multiple local extrema.

For each refined point $\mathbf{p}_k = \left(x_k^*, y_k^{(0)}\right)$ a dynamic programming-based tracing procedure is initiated to generate a polyline.

Pairwise spatial proximity analysis is applied to prevent multiple detections of a single physical structure.

The presented algorithm ensures robust tracing initialization by combining frequency analysis for global structural period estimation with local optimization for precise positioning. The method is particularly effective for analyzing images with periodic linear textures, such as microscopic fiber images, printed circuit boards, or architectural elements.

5 Merging Layers of Overlapping Regions of Close Filtering Directions

Because particle layers may exhibit curvature (see Fig. 5) a critical property influencing catalytic activity regions belonging to the same particle may yield filter responses exceeding the threshold for multiple (typically adjacent) orientations. For this scenario, we developed a graph-based algorithm to merge layers identified in overlapping filter response regions.

For each pair of regions represented by polyline sets, the following are verified:

- Intersection of bounding boxes
- Difference in filter orientations
- Number of points within a specified Euclidean distance

Upon successful matching:

- Vertices of all lines (layers) are merged.
- A Minimum Spanning Tree (MST) is constructed.
- Tree edges exceeding the maximum inter-vertex distance within the lines are pruned.
- On each resulting MST subgraph, the longest path between terminal vertices is identified, subject to:
  - • Minimum length constraint;
  - • Minimum Euclidean distance between endpoints;
  - • Straightness (ratio of direct Euclidean distance between terminal points to path length).

The orientation of the newly formed particle is calculated as the mean orientation, accounting for the equivalence of 0and π. An example of region merging into a particle is shown in Fig. 6.

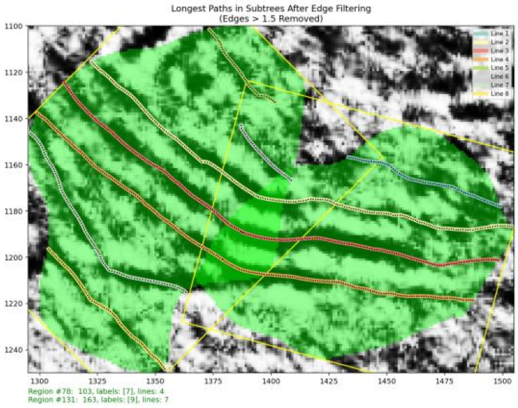

Fig. 6. – Example of constructing lines corresponding to layers of a merged particle

6 Experimental Studies

To evaluate the quality of the constructed lines, we use manually expert-annotated data. Image annotation is an extremely labor-intensive process and may be subject to subjective bias due to the peculiarities of human perception. Currently, we have access to three images on which experts delineated polylines corresponding to nanoplatelets. Each polyline was defined by an arbitrary set of ordered points. The standard CVAT [16] tool was used for annotation.

Lines generated by the algorithm and those drawn by experts were resampled to a fixed number of nodes (set to 30). Quality assessment was based on the root-mean-square distance between corresponding nodes of reference and detected lines. If this distance fell below a predefined threshold, the line was considered correctly detected. Generally, the number of algorithm-detected lines and expert-drawn lines do not match; we computed statistics for three scenarios: (1) an algorithm-proposed line falls within the neighborhood of an expert line (True Positive), (2) an algorithm-proposed line lacks a nearby match among expert lines (False Positive), and (3) an expert line lacks a nearby match among candidate lines (False Negative). The result can thus be represented as a standard confusion matrix excluding the True Negative cell. The standard quality metrics in this context are Precision, Recall, and F_1-score.

Results for three image fragments are presented in Fig. 7.

7 Conclusion

Applying automated methods to analyze high-resolution transmission electron microscopy (HRTEM) micrographs of sulfide catalysts reduces data processing labor and minimizes subjective interpretation bias.

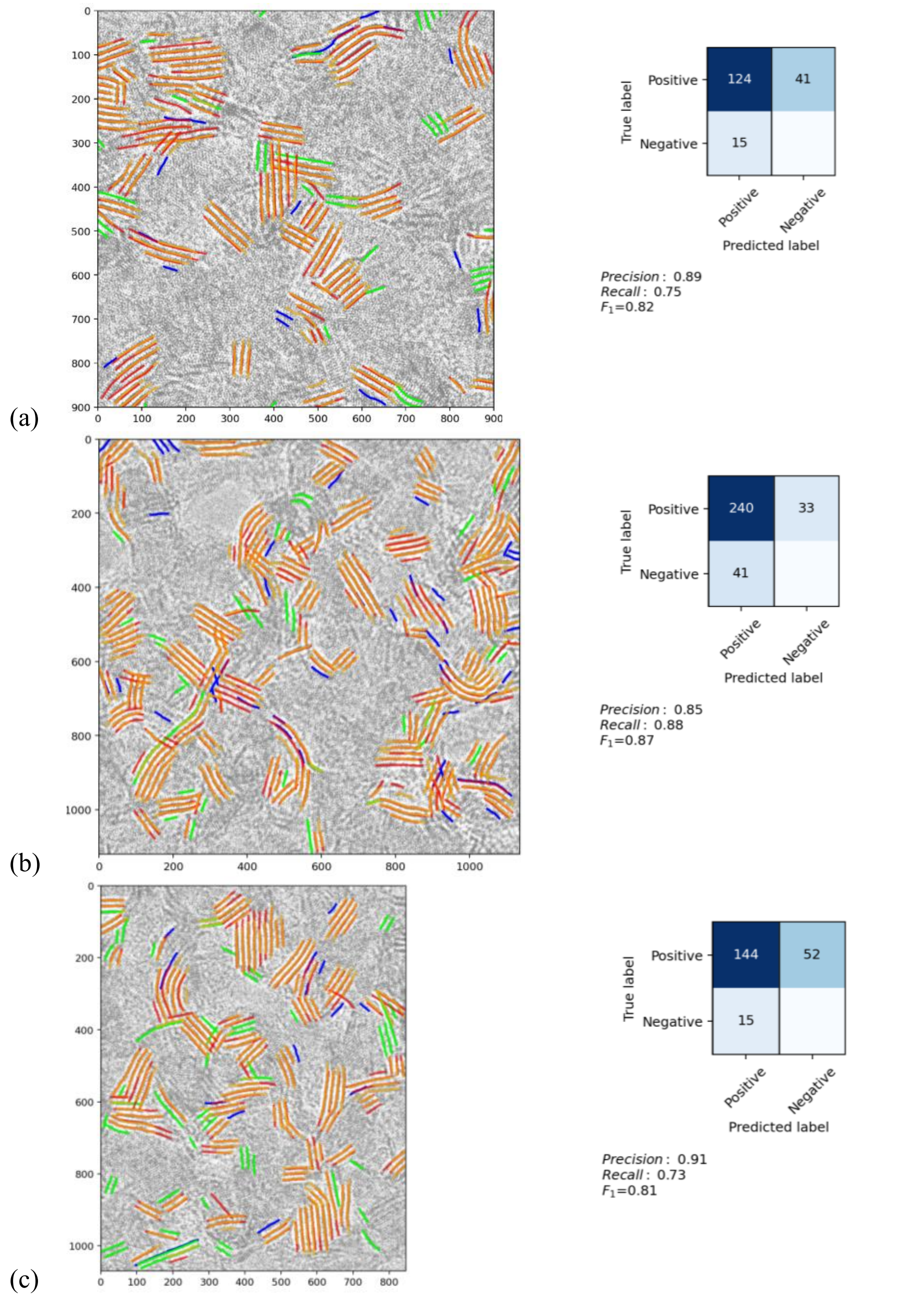

Fig. 7. – Experimental results: (a) annotation and confusion matrix for image C0_0020, (b) annotation and confusion matrix for image C0_0023, (c) annotation and confusion matrix for image C0_0025. Orange and red lines correspond to True Positives; orange lines are detected automatically; red lines represent expert annotation; green lines correspond to False Positives; blue lines correspond to False Negatives.

The problem-solving process is structured into two sequential stages:

- Detection of linear elements corresponding to crystal layers;
- Clustering of detected lines into groups representing sulfide nanoparticles to quantitatively assess morphological characteristics that determine the material's catalytic activity.

The relevance of this study stems from the insufficient exploration of this topic in literature and the constraints imposed on deep learning methods by the high labor cost of preparing annotated datasets.

This work focuses in detail on the first stage of the problem. A line extraction method is proposed, based on spatial Gabor filtering, followed by threshold segmentation, partitioning and filtering of complex regions, and line tracing within identified fragments. To handle curved lines, a procedure for merging layers from overlapping regions of adjacent filter orientations is proposed.

Experimental results demonstrated a high degree of correspondence between automatically detected layers and expert annotations.

The method demonstrates high efficiency in analyzing TEM images of the active phase of molybdenum and tungsten sulfide catalysts (MoS_2, WS_2). The average F_1 – score across all analyzed micrographs was 0.83.

The following image characteristics are accounted for by the algorithm:

- Layered nanoparticle morphology. The active phase forms as stacks of parallel layers 1–5 nm in length and ~0.6 nm thick per layer. The algorithm's spectral module reliably estimates interlayer spacing even in the presence of packing defects and layer curvature.
- Low signal-to-noise ratio. Due to the radiation sensitivity of sulfide structures, imaging is performed at minimal electron doses, reducing contrast. Variational analysis with density-based mask regularization enables layer localization where traditional gradient detectors fail.
- Orientational heterogeneity. Nanoparticles on the support exhibit arbitrary orientations. The orientation normalization stage ensures rotation invariance of detection, which is critical for automated statistical analysis of length and stacking distribution which are key descriptors of catalytic activity.
- Localization of edge sites. Precise positioning of tracing initialization points at intensity minima aligns with the physical model: edge sulfur atoms, responsible for catalysis, appear as dark contrast boundaries in TEM images.

Unfortunately, the labor-intensive nature of manual annotation and the scarcity of publicly available annotated datasets significantly limit the volume of experimental data currently accessible. While we are actively working to annotate additional images for future studies, the primary focus of this work is on the methodological framework itself.

The method's architecture bears a substantive analogy to automated optical inspection (AOI) tasks for printed circuit boards and other periodic structures. The shared mathematical formulation allows the algorithm to be adapted for similar tasks with minimal modifications.

Thus, the proposed approach provides a universal tool for analyzing quasi-periodic linear structures under noisy and geometrically uncertain conditions, with applications in both fundamental nanomaterial research and applied industrial computer vision.

Acknowledgements: The authors acknowledge Dr. Mikhail Boiko, Maria Knyazeva, and Academician Prof. Anton Maximov from the A.V. Topchiev Institute of Petrochemical Synthesis, Russian Academy of Sciences, for providing experimental data and fruitful discussions.

Funding: The research was carried out within the state task № FSFS-2026-0009.

References

1. Payen, E., Hubaut, R., Kasztelan, S., Poulet, O., Grimblot, J.: Morphology Study of MOS2- and WS2-Based Hydrotreating Catalysts by High-Resolution Electron Microscopy. J. Catal. 147, 123–132 (1994). https://doi.org/10.1006/JCAT.1994.1122.
2. Eijsbouts, S., Battiston, A.A., van Leerdam, G.C.: Life cycle of hydroprocessing catalysts and total catalyst management. Catal. Today. 130, 361–373 (2008). https://doi.org/10.1016/J.CATTOD.2007.10.112.
3. Bukhtiyarova, M. V., Vlasova, E.N., Bukhtiyarova, G.A.: Hydroprocessing of biomass feedstock over sulfided CoMo-, NiMo-, and NiW-supported catalysts for bio-jet fuel component production: a review. Sustain. Energy Fuels. 8, 3524–3544 (2024). https://doi.org/10.1039/D4SE00302K.
4. Pakharukova, V.P., Yatsenko, D.A., Gerasimov, E.Y., Vlasova, E., Bukhtiyarova, G.A., Tsybulya, S. V.: Total Scattering Debye Function Analysis: Effective Approach for Structural Studies of Supported MoS2-Based Hydrotreating Catalysts. Ind. Eng. Chem. Res. 59, 10914–10922 (2020). https://doi.org/10.1021/ACS.IECR.0C01254/SUPPL_FILE/IE0C01254_SI_001.PDF.
5. Liu, J., Li, W.Y., Feng, J., Gao, X.: Influence of Ni on the active phase and hydrodenitrogenation and hydrodesulfurization activities of MoS2 catalysts. Journal of Fuel Chemistry and Technology. 49, 1513–1521 (2021). https://doi.org/10.1016/S1872-5813(21)60105-6.
6. Lai, W., Chen, Z., Zhu, J., Yang, L., Zheng, J., Yi, X., Fang, W.: A NiMoS flower-like structure with self-assembled nanosheets as high-performance hydrodesulfurization catalysts. Nanoscale. 8, 3823–3833 (2016). https://doi.org/10.1039/C5NR08841K.
7. Kuchinskaya, T., Mamian, L., Knyazeva, M., Maximov, A.: Hydrodeoxygenation of lignin-derived diphenyl ether on in situ prepared NiMoS catalyst: The effect of sulfur addition on catalyst formation. Appl. Catal. A Gen. 663, (2023). https://doi.org/10.1016/j.apcata.2023.119303.
8. Fraundorf, P., Qin, W., Moeck, P., Mandell, E.: Making sense of nanocrystal lattice fringes. J. Appl. Phys. 98, 114308 (2005). https://doi.org/10.1063/1.2135414.
9. Gamdha, D., Fair, R., Krishnamurthy, A., Gomez, E.D., Ganapathysubramanian, B.: GRATEv2: computational tools for real-time analysis of high-throughput high-resolution TEM (HRTEM) images of conjugated polymers. Mater. Adv. 6, 6820–6842 (2025). https://doi.org/10.1039/D5MA00409H.

10. Yin, C., Wang, Y., Xue, S., Liu, H., Li, H., Liu, C.: Influence of sulfidation conditions on morphology and hydrotreating performance of unsupported Ni–Mo–W catalysts. Fuel. 175, 13–19 (2016). https://doi.org/10.1016/J.FUEL.2016.02.029.
11. Mamian, L.G., Kuchinskaya, T.S., Ziniatullina, A.F., Knyazeva, M.I., Maximov, A.L.: Hydrodeoxygenation of Ether Linkages in Lignin Model Compounds over In Situ Formed NiWS Catalysts. Energy and Fuels. 39, 2035–2047 (2025). https://doi.org/10.1021/ACS.ENERGYFUELS.4C04798/SUPPL_FILE/EF4C04798_SI_001.PDF.
12. Gabor, D.: Theory of communication. Part 1: The analysis of information. Journal of the Institution of Electrical Engineers - Part III: Radio and Communication Engineering. 93, 429–441 (1946). https://doi.org/10.1049/JI-3-2.1946.0074.
13. Wang, H., Zhang, H., Ray, N.: Clump splitting via bottleneck detection and shape classification. Pattern Recognit. 45, 2780–2787 (2012). https://doi.org/10.1016/J.PATCOG.2011.12.020.
14. Miró-Nicolau, M., Moyà-Alcover, G., González-Hidalgo, M., Jaume-i-Capó, A.: Improving concave point detection to better segment overlapped objects in images. Multimed. Tools Appl. 83, 24339–24359 (2024). https://doi.org/10.1007/S11042-023-15382-1/TABLES/7.
15. Liao, M., Zhao, Y. qian, Wang, W., Zeng, Y. zhan, Yang, Q., Shih, F.Y., Zou, B. ji: Efficient liver segmentation in CT images based on graph cuts and bottleneck detection. Physica Medica. 32, 1383–1396 (2016). https://doi.org/10.1016/J.EJMP.2016.10.002.
16. Leading Image & Video Data Annotation Platform | CVAT, https://www.cvat.ai/, last accessed 2026/05/21.